

# Growing highly pure semiconducting carbon nanotubes by electrotwisting the helicity

Jiangtao Wang<sup>1</sup>, Xiang Jin<sup>1</sup>, Zebin Liu<sup>1</sup>, Guo Yu<sup>1</sup>, Qingqing Ji<sup>2</sup>, Haoming Wei<sup>1</sup>, Jin Zhang<sup>1</sup>, Ke Zhang<sup>1</sup>, Dongqi Li<sup>1</sup>, Zi Yuan<sup>1</sup>, Jiachen Li<sup>1</sup>, Peng Liu<sup>1\*</sup>, Yang Wu<sup>1</sup>, Yang Wei<sup>1</sup>, Jiaping Wang<sup>1,3</sup>, Qunqing Li<sup>1,3</sup>, Lina Zhang<sup>1</sup>, Jing Kong<sup>2\*</sup>, Shoushan Fan<sup>1,3</sup> and Kaili Jiang<sup>1,3\*</sup>

**Carbon nanotubes (CNTs) are anticipated to be the successor of silicon in next-generation integrated circuits. However, one great challenge to the practical application of this concept is the need to grow horizontal semiconducting CNT arrays with very high purity. Here we show that this roadblock can be eliminated by switching the direction of an applied electric field during synthesis. This electro-renucleation approach twists the chirality of the CNTs to produce nearly defect-free s-CNTs horizontally aligned on the substrate with less than 0.1% residual metallic CNT. In principle, this residual percentage can be further reduced to less than 1 ppm simply by tuning the CNTs' diameters to around 1.3 nm. Electro-renucleation thus offers a potential pathway to practical applications of CNT electronics and opens up a new avenue for large-scale selective synthesis of semiconducting CNTs and other nanomaterials.**

CNTs are thought to be the successor of silicon in the post-Moore's law era<sup>1</sup>. Proof-of-concept devices and systems<sup>2</sup>, such as CNT-based computers<sup>3</sup>, three-dimensional chips<sup>4</sup> and transistors with a 5 nm gate length<sup>5</sup> or a 40 nm footprint<sup>6</sup>, have been successfully demonstrated. The greatest impediment to the industrial application of CNTs in electronics has been the requirement of obtaining pure semiconducting CNT (s-CNT) horizontal arrays<sup>7</sup>. Two approaches have been developed in an effort to meet this challenge. The first approach is post-growth separation based on density-gradient centrifugation<sup>8</sup> or chromatography<sup>9</sup>. This can produce high yields of highly pure s-CNTs; however, drawbacks, including very short product lengths (<1  $\mu\text{m}$ ) and abundant defects, dramatically degrade the quality of said s-CNTs. The second approach, direct synthesis via conventional chemical vapour deposition (CVD), can produce long and defect-free s-CNT horizontal arrays with high quality. Over the past 20 years, CVD methodologies for the selective growth of s-CNTs have focused on selective etching<sup>10–13</sup>, molecular seeding<sup>14</sup> and catalyst design<sup>15–19</sup>—exploiting differences in thermodynamics and growth kinetics between s-CNTs and metallic CNTs (m-CNTs)<sup>20,21</sup>. However, even with the most-effective catalyst design method, the lowest proportion of residual m-CNTs that has been reported to date is still 1.3% (ref. <sup>19</sup>)—which is far in excess of the requirements of the semiconductor industry.

During a conventional CVD synthesis, the catalyst plays the key role in determining the chirality of the grown nanotube. In most cases, nanotube chirality remains the same throughout the synthesis process<sup>22</sup>. For this reason, catalyst design has been the primary means used for achieving preferential growth of s-CNTs or CNTs with a certain chirality<sup>19,23–25</sup>. On the other hand, nanotube chirality can be altered through a renucleation process if a perturbation occurring during CNT growth results in the formation of a chiral junction (with an associated extra energy cost<sup>26–28</sup>) in the nanotube. But the preferential growth of s-CNTs through the controlled change of nanotube chirality has not to date been reported.

The recently discovered fact that CNTs and their catalysts are spontaneously charged during Fe-catalysed CVD<sup>29–33</sup> (particularly, spontaneous negative-charging when hydrocarbon gas is used as a carbon source<sup>29</sup>) suggests that an electric field might be used as a perturbation to initiate the renucleation process and twist the helicity of the CNTs in a controllable manner.

The electro-renucleation (ERN) approach reported herein can significantly amplify the renucleation barrier difference between m-CNTs and s-CNTs, so that m-CNTs may be twisted into semiconducting ones by switching the direction of an applied electric field. This has resulted in the production of s-CNT arrays with very high purity, and field-effect transistors (FETs) fabricated using said ERN-grown s-CNT arrays show much better performances than those previously reported. Further, theoretical analysis indicates that s-CNT arrays with as low as 1 ppm residual m-CNT contamination can be achieved by further restricting the diameters of the CNTs. This highly efficient and highly operable ERN approach should enable large-scale selective synthesis of s-CNTs in the near future, which in turn should provide a foundation for industrial applications of high-performance CNT FETs.

## Results

**Twisting the chirality of CNTs from metallic to semiconducting by ERN.** Figure 1a depicts the ERN system: the substrate, an ST-cut single quartz crystal with Fe catalyst strips<sup>34</sup>, is placed between a pair of graphite electrodes with its lattice-guided growth direction parallel to the electric field. Figure 1b illustrates the steps involved in the renucleation process. After the random nucleation of CNTs at a temperature of 950 °C, an electric field is applied to (lightly) positively charge the catalyst particles. This results in most m-CNTs acquiring a modest positive charge while s-CNTs remain close to charge neutral due to their bandgap. At time  $t_0$ , the polarity of the electric field is reversed to (heavily) negatively charge the catalyst particles. This reversal acts to perturb the catalyst particles and

<sup>1</sup>State Key Laboratory of Low-Dimensional Quantum Physics, Department of Physics and Tsinghua-Foxconn Nanotechnology Research Center, Tsinghua University, Beijing, China. <sup>2</sup>Department of Electrical Engineering and Computer Science, Massachusetts Institute of Technology, Cambridge, MA, USA.

<sup>3</sup>Collaborative Innovation Centre of Quantum Matter, Beijing, China. \*e-mail: [PengLiu@tsinghua.edu.cn](mailto:PengLiu@tsinghua.edu.cn); [jingkong@mit.edu](mailto:jingkong@mit.edu); [JiangKL@tsinghua.edu.cn](mailto:JiangKL@tsinghua.edu.cn)

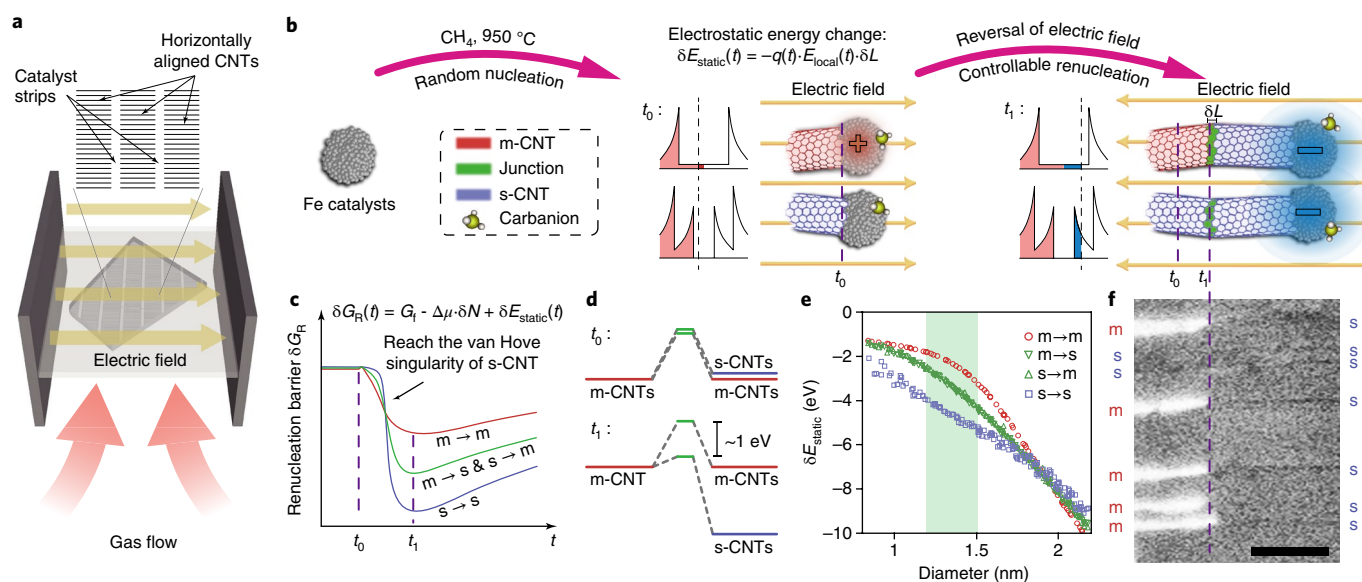


**Fig. 1 | Controllably twisting the chirality of CNTs from metallic to semiconducting.** **a**, Schematic diagram of the ERN system. **b**, Twisting the chirality of CNTs by reversing the electric field to grow s-CNTs. **c**, Renucleation barrier change as a function of time after the electric field is reversed. **d**, At time  $t_0$ , when the electric field is reversed, the renucleation energy barrier of m-CNT  $\rightarrow$  s-CNT (m  $\rightarrow$  s) is slightly higher than that of m-CNT  $\rightarrow$  m-CNT (m  $\rightarrow$  m); at time  $t_1$  (see also the DOS and carrier-filling diagram in **b**), when the charge stored in s-CNT greatly exceeds that in m-CNT, the m  $\rightarrow$  s renucleation barrier becomes much lower than that of m  $\rightarrow$  m. **e**, Calculated electrostatic energy change versus CNT diameter before twisting (for each chirality change, the diameter remains almost constant). **f**, SEM image of the CNTs with chirality changing from metallic to semiconducting. Bright lines and dark lines indicate m-CNTs and s-CNTs, respectively (they are also labeled by red 'm' and blue 's'). Scale bar, 500 nm.

form a chiral junction, complete with an extra energy cost<sup>26,27</sup>, which connects two different chiralities. In the presence of an electric field, the renucleation barrier may be expressed as

$$\delta G_R(t) = G_f - \Delta\mu \cdot \delta N + \delta E_{\text{static}}(t) \quad (1)$$

where  $G_f$  is the formation energy of the junction,  $\Delta\mu$  is the chemical potential difference between carbon being dissolved in the catalyst and carbon bound in the nanotube lattice,  $\delta N$  is the number of carbon atoms in the junction, and  $\delta E_{\text{static}}(t)$  is the electrostatic energy change during renucleation. Since the renucleation time ( $\sim 5 \times 10^{-4}$  s, as estimated from the typical growth rate of  $\sim 30 \mu\text{m min}^{-1}$  and a chiral junction length of  $\sim 0.25$  nm) is much shorter than the charging time ( $\sim 0.5$  s, based on measurements of the charging current), the Fermi level of the CNTs should remain roughly constant during renucleation. The decrease in electrostatic energy in the nano-catalytic system will be equal to the work done by the local electric field, thus  $\delta E_{\text{static}}(t) = -q(t)E_{\text{local}}(t) \cdot \delta L$ , in which  $\delta L$  is a vector representing the elongation of the CNT during renucleation,  $q(t)$  is the time-dependent charge of the catalyst particle region, and  $E_{\text{local}}(t)$  is the vector sum of correlated local electric field. Both m-CNTs and s-CNTs have only one atomic shell layer in which the external electric field is not completely screened by the atomic electron density. The induced charge in a particular catalyst region is determined by both the applied electric field and the local density of states (LDOS). Different LDOS lead to different  $q(t)$  for each type of chiral junction—metallic to metallic (m  $\rightarrow$  m), metallic to semiconducting (m  $\rightarrow$  s) (or semiconducting to metallic (s  $\rightarrow$  m)) and semiconducting to semiconducting (s  $\rightarrow$  s)—the charge  $q(t)$  is different because of their LDOS. Since the energy levels of the electron in carbanions  $\text{CH}_3^-$  ( $-0.08$  eV; ref.<sup>35</sup>) and  $\text{CH}_2^-$  ( $-0.21$  eV; ref.<sup>36</sup>) are higher than that in Fe catalysts ( $-4.5$  eV), the catalysts will be negatively charged spontaneously as reported previously<sup>29</sup>. Because of this, the Fermi level is shifted to the right of the neutral point during the growth (Fig. 1b). When the catalysts are positively

charged, the Fermi level is located in the bandgap of s-CNTs, and m-CNTs are charged more heavily than s-CNTs. However, when the catalysts are negatively charged, the Fermi level is raised to maximum value and over the first van Hove singularity of s-CNTs at the time of  $t_1$  ( $t_1 - t_0$  is about 100 to 500 ms, depending on the area and the distance of the electrodes). In this case, the s-CNT electronic density of states (DOS) becomes an order of magnitude larger than the m-CNT DOS<sup>37</sup>, so that many more extra electrons can be stored in the s-CNT catalyst region compared to that of the m-CNTs. The net charge storability of a chiral junction should be the average of those for the two connected chiralities<sup>27</sup>. According to the formula above, during the formation of the chiral junction, the renucleation barrier will be lowered by the increased amount of charge stored in the catalyst region. Figure 1c plots the time dependence of the renucleation barrier for the three different types of junctions: m  $\rightarrow$  m, m  $\rightarrow$  s (and s  $\rightarrow$  m) and s  $\rightarrow$  s. Prior to time  $t_0$ , the renucleation barriers are too high to precipitate a chirality change. However, by time  $t_1$ , the charging of the catalyst regions have significantly lowered the renucleation barriers. The reduction of the renucleation barrier for the m  $\rightarrow$  s junction far exceeds that of the m  $\rightarrow$  m junction. A perturbation provided by the change of outside electric field overcomes the lower renucleation barrier, leading to a selective twist in the helicity. Figure 1d illustrates how the m  $\rightarrow$  m, and m  $\rightarrow$  s junction barriers change between times  $t_0$  and  $t_1$ , which indicates that m-CNTs tend to be twisted to s-CNTs. In contrast, the renucleation barrier of s  $\rightarrow$  s junction is much lower than that of s  $\rightarrow$  m junction, thus s-CNTs remain semiconducting. Figure 1e plots calculated values for the decrease in electrostatic energy for each type of chirality change as a function of the nanotube diameter (the diameter remains approximately constant, see Supplementary Note 1 and Supplementary Fig. 1; details of this calculation are provided in Methods, including a discussion of behaviour of the Fermi distribution function at high temperatures and an estimate of the maximum rise of the Fermi level due to the reversal of the electric field in Supplementary Fig. 2). Differences in the amount by

which the electrostatic energy decreases are most pronounced in the 1.2 nm to 1.5 nm diameter range. As shown in the scanning electron microscope (SEM) image (Fig. 1f), the CNTs on quartz change from metallic (bright) to semiconducting (dark) when the direction of the electric field is reversed. This SEM image contrast between the single-walled m-CNTs and s-CNTs on the quartz substrate results from differences in the secondary electron emission rates brought about by the different charge densities<sup>38–41</sup>. Furthermore, electrostatic force microscope (EFM) is used to characterize this chirality change<sup>42</sup>, showing similar results to SEM (Supplementary Fig. 3). Figure 2a (2c) shows an SEM image of an FET fabricated on a bright m-CNT (dark s-CNT). The corresponding electric measurements in Fig. 2b (2d) confirm that the bright CNTs are metallic and the dark CNTs are semiconducting.

We found that the percentage of the CNTs undergoing a chirality change is positively correlated with the amplitude of the parallel component of the perturbing (changing) electric field. No chirality changes were observed when CNTs were grown in either an electric field with only a non-zero perpendicular component or one whose parallel component remained constant (these situations are depicted in Supplementary Fig. 4). Since the absolute strength of the applied electric field is limited by the breakdown voltage of about

$300 \text{ V mm}^{-1}$  under growth conditions, to maximize the perturbation, it is better to reverse the direction of the electric field than to turn the electric field on and off.

**Highly pure s-CNT horizontal arrays grown by ERN.** Growth results under three different electric field regimes were compared to demonstrate the advantages of the ERN method described above. Regime 1 utilized a conventional growth recipe with no electric field applied to the CVD system. Resulting arrays were admixtures of s-CNTs and m-CNTs, an example of which is presented in Fig. 2e (therein the region boxed by a yellow line is the catalyst strip and the upward arrow indicates the growth direction). It is obvious from their brightness that a large portion of CNTs are metallic tubes. To show the dark s-CNTs in this mixed-CNT array more clearly, an ultra-long CNT<sup>43</sup> was placed flat on the array oriented more-or-less diagonally across the mixed-CNT array. Then short Schottky barriers appear at the intersections of the dark tubes and the ultra-long CNT (these are enclosed by blue circles in Fig. 2e). Regime 2 enacted the ERN method developed in this study of applying an electric field and then reversing it to twist the helicity during the growth. Results are seen in Fig. 2f, where clearly the bright m-CNTs have been twisted into dark s-CNTs. The hetero-

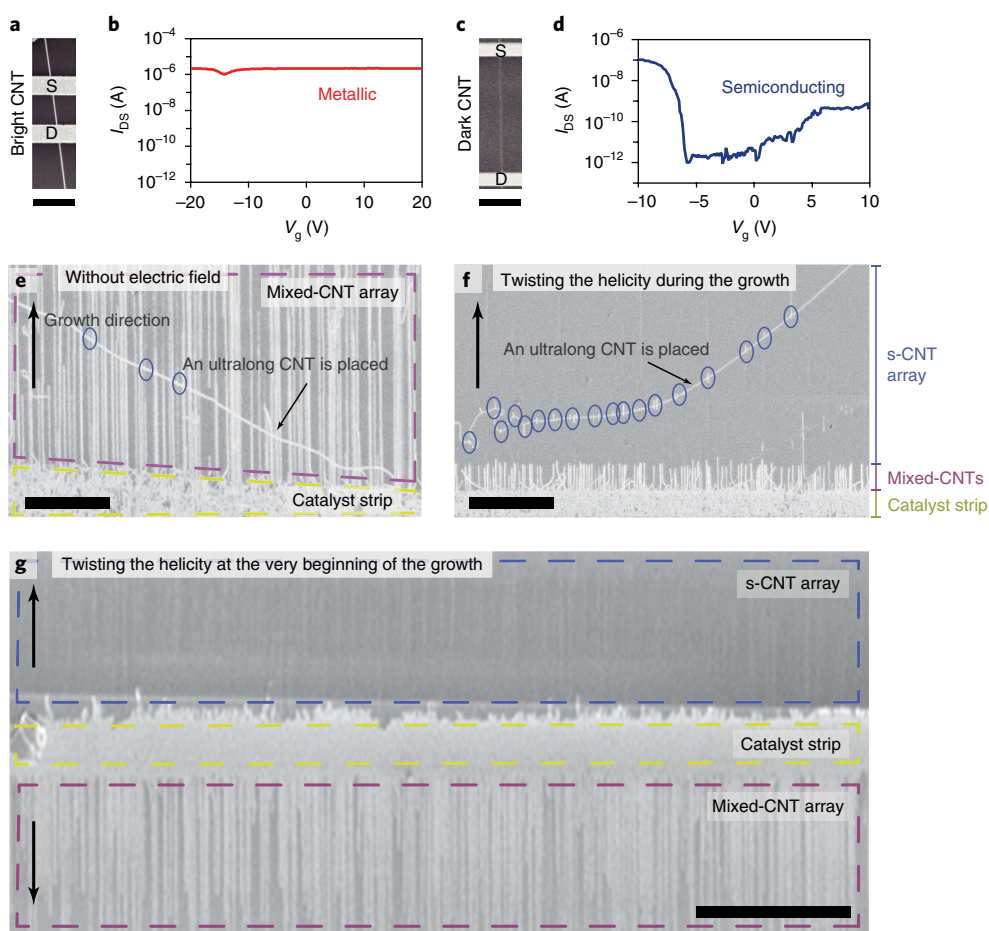


**Fig. 2 | High-purity s-CNT array grown by ERN method.** **a, c**, SEM image of a bright m-CNT (**a**) and a dark s-CNT (**c**). **b, d**, The corresponding transfer characteristic curves of the CNTs in **b** and **d**, respectively. Bias voltage is 1V. **e–g**, SEM images of a CNT array grown on quartz synthesized without an electric field (**e**), with an electric field twisting the helicity during growth (**f**) and with electric field twisting the helicity at the very beginning of the growth (**g**). The upward and downward arrows in these images indicate the growth directions, whereas the rectangular regions bounded by dashed yellow lines in **e** and **g** are the catalyst strips. Ultra-long CNTs are placed horizontally across a mixed-CNT array in **e** and a s-CNT array in **f**. The Schottky barriers, enclosed by blue circles, at almost every intersection between the ultra-long CNTs and the dark tubes, indicate the presence of s-CNTs. Scale bars, 4  $\mu\text{m}$  (**a**), 8  $\mu\text{m}$  (**c**), 20  $\mu\text{m}$  (**e–g**).

junctions align perpendicularly to the growth direction (resulting from the almost simultaneous nucleations and similar growth rates of the CNTs under a strong electric field; see Supplementary Note 2 and Supplementary Fig. 5<sup>44</sup> and 6). As before, an ultra-long CNT was placed across the CNT array, and all intersections of the ultra-long CNT and the aligned CNTs possessed short Schottky barriers (again enclosed by blue circles), confirming that no m-CNTs existed after the ERN process. Finally, regime 3 reverses the electric field at the very beginning of the growth. The SEM image of the resulting as-grown CNT array shown in Fig. 2g, wherein all the CNTs enclosed by the blue-rectangle are clearly much darker than those enclosed by the purple-rectangle. SEM imaging techniques<sup>38–41</sup> demonstrate that all the CNTs inside the blue-edged rectangular area (about 1,200 tubes) are semiconducting, while the CNTs grown downward inside the purple-edged rectangular area remain a mixture of m-CNTs and s-CNTs. This mixture growth can be easily terminated by a trench etched on the quartz substrate (see Supplementary Fig. 7). SEM images under several magnifications are shown in Supplementary Figs. 8–10.

## Discussion

For further verification of the selectivity, we measured the electrical properties and Raman spectra of the ERN-grown s-CNT array. The inset of Fig. 3a shows the SEM image of an FET formed by transferring the ERN-grown s-CNT array onto an SiO<sub>2</sub>/Si substrate; herein false colour is used to label the source and drain electrodes. The corresponding transfer characteristic curve is plotted in Fig. 3a. This s-CNT-array FET possesses a high on/off ratio (10<sup>6</sup>) and a two orders of magnitude higher on-current than the FET fabricated on an individual s-CNT (as shown in Fig. 2d). This confirms the high selectivity of the ERN method. Figure 3b gives a comparison of the on/off ratio of s-CNT-array FETs produced in this study to those previously reported, from which the exact purity of ERN-grown s-CNT array is found to be higher than 99.6% (Supplementary Fig. 11). The results of this study clearly represent a significant leap forward in improving the purity of s-CNT arrays. Furthermore, source and drain electrodes were prefabricated with a separation distance of 6 μm on the quartz substrate, and the s-CNTs were grown directly in the channels to prevent the decrease of on-state current induced from conventional transfer steps (PMMA residue). Using ionic liquid as the gate dielectric layer results in an on-state current for one tube of 1.4 μA with a 1 V bias (see Supplementary Fig. 12, 6 μm channel length). The on-state current of per ERN-grown s-CNT is similar to that previously reported<sup>45</sup>, confirming the high quality of our tubes. In addition, the Raman spectra of the ERN-grown s-CNT array shown in Fig. 4a (and Supplementary Fig. 13) exhibit typical Lorentzian lineshapes in the G-band, and the D peak to

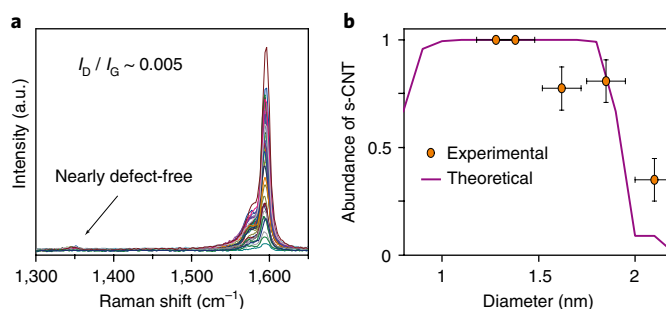


**Fig. 4 | Raman characterization of ERN-grown s-CNT array.** **a**, Raman spectra of ERN-grown s-CNT array with the excitation wavelength of 514 nm. a.u., arbitrary units. **b**, Experimental values and theoretical curve for s-CNT abundance versus nanotube diameter. The uncertainty of the diameters (horizontal error bars) is roughly estimated to be  $\pm 0.1$  nm according to the Raman peak width of the radial breathing mode (RBM). The uncertainty of the abundance (vertical error bars) comes from the limited numbers of the CNTs, which is roughly estimated to be  $\pm 0.1$ .

G peak intensity ratio is  $\sim 0.005$ , indicating, respectively, a high level of purity and a very low incidence of defects for the ERN-grown s-CNT array<sup>37</sup>. As illustrated in Fig. 1e, the difference between the renucleation barriers for the  $m \rightarrow m$  and  $m \rightarrow s$  junctions depends on the diameters of CNTs. In this study, catalysts for CNT growth were obtained by evaporating 2 Å Fe, resulting in a distribution of CNT diameters between 1–2 nm. Use of a thicker Fe catalyst (such as 5 Å) would result in a wider distribution of CNT diameters, with more tubes falling outside the useful range indicated in Fig. 1e, thus rendering the ERN twisting method less effective. Figure 4b gives the results based on Raman spectroscopy (utilizing radial breathing mode (RBM) peaks, see Supplementary Fig. 14) for the s-CNT abundance at different CNT diameters of a sample with somewhat lower purity. A theoretical estimation for the s-CNT abundance as a function of the tube diameter may be obtained using the renucleation barrier difference versus CNT diameter relationship. The s-CNT abundance, plotted in Fig. 4b, is estimated to be  $P = 1 - 0.33 \exp\left(-\frac{\delta G_{m \rightarrow m} - \delta G_{m \rightarrow s}}{kT}\right) - 0.67 \exp\left(-\frac{\delta G_{s \rightarrow m} - \delta G_{s \rightarrow s}}{kT}\right)$ , where  $k$  is Boltzmann's constant and  $T$  represents the growth temperature. Figure 4b indicates that the results from experimental data agree reasonably well with this theoretical curve, and also that both theoretical and experimental values point toward higher selectivity when the diameters of the CNTs are more narrowly confined (to the preferred zone of Fig. 1e). Under the growth conditions of this study, the highest s-CNT abundance is calculated to be 99.9999% with a nanotube diameter of 1.3 nm.

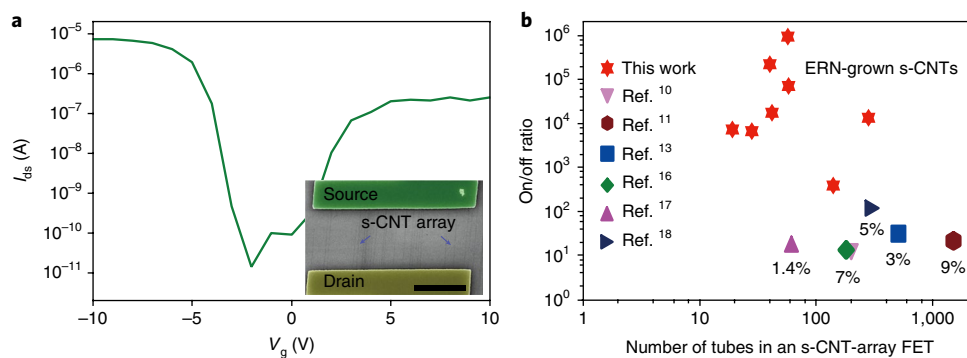


**Fig. 3 | FET fabricated on ERN-grown s-CNT array.** **a**, The transfer characteristic curves of the s-CNT-array FET with a bias voltage of 1 V. Inset is the SEM image of an FET fabricated on ERN-grown s-CNT array, in which false colour is used to label source and drain electrodes. Scale bar, 3 μm. **b**, A comparison of the on/off ratio of s-CNT-array FETs from the current study to those previously reported (the residual m-CNT percentages are as indicated).

In conclusion, our discovery demonstrates that the extra electrons in the region of catalyst particles play a more prominent role in modulating the renucleation barrier, which leads to a high-selectivity renucleation of s-CNTs. Nearly-defect-free s-CNT arrays with residual m-CNTs less than 0.1% (estimated from SEM images) are directly obtained as a result of ERN. With more careful tuning of the diameter of the catalyst particles, we anticipate that the growth of s-CNT array with the abundance of 99.9999% to meet the requirement of semiconductor industry will be eventually achieved in the near future.

## Methods

**Preparation of the catalyst strips on ST-cut single crystal quartz.** The catalyst strips on quartz are prepared by lithography and deposition of 0.2 nm Fe with an electron-beam evaporator.

**Growth of s-CNT array.** To grow s-CNTs, the furnace temperature is ramped up to 950 °C within 10 min in an atmosphere of H<sub>2</sub> and CH<sub>4</sub> with flow rates of 500 sccm and 200 sccm, respectively. Then the gas flow is switched to 5 sccm H<sub>2</sub> and 2 sccm CH<sub>4</sub> to initiate the growth; meanwhile, an electric field (200 V mm<sup>-1</sup>) is applied for ~20–200 s. Then reversed electric field pulses are used to twist the helicity of CNTs during the growth (see Supplementary Note 3, Supplementary Figs. 15a and 16). Finally, after growing for ~0–4 min, the sample is withdrawn from the high temperature area, placed in an environment of 1,000 sccm Ar and cooled down quickly to room temperature within 8 min.

**Calculation of electrostatic energy change.** According to the definition of electrostatic energy,  $\delta E_{\text{static}}(t) = -q(t)E_{\text{local}}(t) \cdot \delta L$ , in which  $\delta L$  is the vector of the elongation of the CNT during the renucleation,  $q(t)$  is the time-dependent charge in the region of catalyst particle, and  $E_{\text{local}}(t)$  is the corresponding local electric field vector. According to Gauss' theorem,  $2e_0 E_{\sigma} \Delta A = \sigma(t) \Delta A$  and  $e_0(E_s + E_{\sigma}) \Delta A = \sigma(t) \Delta A$ , in which  $E_s$  is the electric field caused by the surface charge on the element of area  $\Delta A$ ,  $E_s$  is the local surface electric field,  $\sigma(t)$  is the surface density of  $q(t)$  and  $e_0$  the vacuum permittivity. Thus  $E_s = \frac{\sigma(t)}{2e_0}$ .  $q(t)E_{\text{local}}(t) \cdot \delta L = \sigma(t)E_s \delta V$ , where the increased volume of the tube is  $\delta V = \pi R^2 \delta L$ ; hence, the maximum electrostatic energy change is  $\delta E_{\text{static}} = -\frac{\pi R^2 \sigma_{\text{max}}^2}{2e_0} \delta L$ , in which  $\delta L$  is the length of the junction (0.25 nm) and  $R$  is the radius of the tube. The surface charge density is the integral of the product of the element charges, the LDOS of the junction and the Fermi distribution function  $f(E)$  at a temperature of 1,200 K, that is,  $\sigma_{\text{max}} = e \left[ \int_0^{+\infty} \text{LDOS}(E) f(E - E_{\text{Fmax}}) dE - \int_{-\infty}^0 \text{LDOS}(E) f(E_{\text{Fmax}} - E) dE \right]$ . In order to simplify the calculation of the renucleation energy, the LDOS of the junction is approximated by the average of the DOS before and after the junction (similar to the results in ref. 27). The Fermi level is chosen to be 0.35 eV above the average of the spontaneously charging levels of the growth of CNT before and after the junction as discussed in the following subsection.

**Determination of the variation of the renucleation barrier.** Before the reversal, the catalyst particles of upward-grown CNTs in Fig. 1f is positively charged by the electric field but also partially neutralized by spontaneously charging. Meanwhile, the thermal ionized H<sup>+</sup> are repelled by the catalyst particles and attracted by the negative electrode. When the electric field is reversed, the catalyst particles gradually become negatively charged with a charging time ( $t$ ), resulted from the redistribution of thermal ions between the electrodes. Consequently, the Fermi level rises until the extra electrons tunnel to the attracted H<sup>+</sup> ions. Next, the Fermi level is gradually drawn back down to the spontaneously charging level, and an equilibrium between electrons transferring from the carbanions and those tunnelling to H<sup>+</sup> ions is established<sup>29</sup>. This discharge time is labelled as ( $t^*$ ). The variation curve of the Fermi level, the charge and the renucleation barrier are given by the following equations:

$$E_{\text{F}}(t) = E_{\text{Fmax}} \left( 1 - e^{-\frac{t}{\tau}} \right) e^{-\frac{t}{\tau}}$$

$$q(t) \propto \sigma(t) = -e \left( \int_0^{+\infty} \text{LDOS}(E) f(E - E_{\text{F}}(t)) dE - \int_{-\infty}^0 \text{LDOS}(E) f(E_{\text{F}}(t) - E) dE \right)$$

$$\delta G_{\text{R}}(t) = G_{\text{F}} - \Delta \mu \cdot \delta N - \frac{\pi R^2 \delta L}{2e_0} \sigma^2(t)$$

The maximum increase in the Fermi level caused by the external electric field is estimated by measuring a self-discharging current. When a stronger electric field of

220 V mm<sup>-1</sup> is reversed for 10 s, an irregularly shaped area is observed on the SEM image (Supplementary Fig. 2a). The corresponding Raman spectra (Supplementary Fig. 2b) indicate that the irregular area is amorphous carbon. Presumably the amorphous carbon is deposited by the self-discharging current from the tip of CNTs when the Fermi level in catalyst particle region is so high that a large number of electrons are emitted. With the assumption that each deposited C atom results from one CH<sub>4</sub> molecule ionized by a discharged electron, a lower limit on the self-discharge current can be estimated as  $I \approx \frac{ATe}{a_{\text{C-C}}^3 - \Delta t}$ , where  $A$  is the area (~30 μm<sup>2</sup>),  $T$  is the thickness of the amorphous carbon (measured by a step meter, ~100 nm),  $e$  represents the element's charge,  $a_{\text{C-C}}$  is the length of the C-C bond, and  $\Delta t$  is the deposition time (10 s). According to the Fowler–Nordheim formula<sup>46</sup>:

$$J = \frac{e^3 E_{\text{local}}^2}{8\pi h(\phi - E_{\text{F}})} \exp \left( -\frac{4\sqrt{2m}(\phi - E_{\text{F}})^{3/2}}{3heE_{\text{local}}} \right),$$

where  $J$  is the current density,  $E_{\text{local}}$  is the local electric field,  $m$  is the effective electron mass and  $\Phi$  is the work function. Using data on the DOS of CNTs quoted from S. Maruyama's website ([http://www.photon.t.u-tokyo.ac.jp/~maruyama/kataura/ID\\_DOS.html](http://www.photon.t.u-tokyo.ac.jp/~maruyama/kataura/ID_DOS.html)),  $I$  can be used to find the average raised value of the Fermi level. For example, the value is about 0.7 eV for CNTs with chiral indices of (12,7). Thus, the maximum raised value of the Fermi level may be reasonably approximated as 0.35 eV above its spontaneously charging level (0.4 eV). According to above analysis, in the region of catalyst particle where most of the electrons are aggregated, the typical charge density is about 0.022 electron per carbon atom (3.2 electrons per nm) for electro-twisting the helicity (11,8) → (12,7).

**SEM images.** The SEM (FEI NOVA 450) was operated at 1 kV (Figs. 1 and 2) or 10 kV (Fig. 3) with a working distance of 5 mm (refs. 38–41).

**FETs fabricated on s-CNT arrays.** The as-grown s-CNT arrays are transferred onto a marked Si substrate with a 100 nm SiO<sub>2</sub> layer by using poly(methyl methacrylate) (PMMA). After removal of the PMMA in acetone, another layer of PMMA is spin-coated onto the silicon slice as the resist. Electrodes are patterned and formed via electron beam lithography (EBL), followed by deposition of a 50-nm-thick Pd film and a standard lift-off process.

**Data availability.** The data that support the plots within this paper and other findings of this study are available from the corresponding author upon reasonable request.

Received: 19 December 2017; Accepted: 20 March 2018;

Published online: 23 April 2018

## References

- De Volder, M. F., Tawfik, S. H., Baughman, R. H. & Hart, A. J. Carbon nanotubes: present and future commercial applications. *Science* **339**, 535–539 (2013).
- Bachtold, A., Hadley, P., Nakanishi, T. & Dekker, C. Logic circuits with carbon nanotube transistors. *Science* **294**, 1317–1320 (2001).
- Shulaker, M. M. et al. Carbon nanotube computer. *Nature* **501**, 526–530 (2013).
- Shulaker, M. M. et al. Three-dimensional integration of nanotechnologies for computing and data storage on a single chip. *Nature* **547**, 74–78 (2017).
- Qiu, C. et al. Scaling carbon nanotube complementary transistors to 5-nm gate lengths. *Science* **355**, 271–276 (2017).
- Cao, Q., Tersoff, J., Farmer, D. B., Zhu, Y. & Han, S. J. Carbon nanotube transistors scaled to a 40-nanometer footprint. *Science* **356**, 1369–1372 (2017).
- Franklin, A. D. The road to carbon nanotube transistors. *Nature* **498**, 443–444 (2013).
- Arnold, M. S., Green, A. A., Hulvat, J. F., Stupp, S. I. & Hersam, M. C. Sorting carbon nanotubes by electronic structure using density differentiation. *Nat. Nanotechnol.* **1**, 60–65 (2006).
- Tu, X., Manohar, S., Jagota, A. & Zheng, M. DNA sequence motifs for structure-specific recognition and separation of carbon nanotubes. *Nature* **460**, 250–253 (2009).
- Zhou, W., Ding, L., Yang, S. & Liu, J. Synthesis of high-density, large-diameter, and aligned single-walled carbon nanotubes by multiple-cycle growth methods. *ACS Nano* **5**, 3849–3857 (2011).
- Kang, L., Zhang, S., Li, Q. & Zhang, J. Growth of horizontal semiconducting SWNT arrays with density higher than 100 tubes/mum using ethanol/methane chemical vapor deposition. *J. Am. Chem. Soc.* **138**, 6727–6730 (2016).
- Hong, G. et al. Direct growth of semiconducting single-walled carbon nanotube array. *J. Am. Chem. Soc.* **131**, 14642–14643 (2009).
- Ding, L. et al. Selective growth of well-aligned semiconducting single-walled carbon nanotubes. *Nano Lett.* **9**, 800–805 (2009).
- Liu, B. et al. Nearly exclusive growth of small diameter semiconducting single-wall carbon nanotubes from organic chemistry synthetic end-cap molecules. *Nano Lett.* **15**, 586–595 (2015).

15. Zhang, S., Tong, L., Hu, Y., Kang, L. & Zhang, J. Diameter-specific growth of semiconducting SWNT arrays using uniform Mo<sub>2</sub>C solid catalyst. *J. Am. Chem. Soc.* **137**, 8904–8907 (2015).
16. Zhang, S. et al. Selective scission of C–O and C–C bonds in ethanol using bimetal catalysts for the preferential growth of semiconducting SWNT arrays. *J. Am. Chem. Soc.* **137**, 1012–1015 (2015).
17. Qin, X. et al. Growth of semiconducting single-walled carbon nanotubes by using ceria as catalyst supports. *Nano Lett.* **14**, 512–517 (2014).
18. Kang, L. et al. Growth of close-packed semiconducting single-walled carbon nanotube arrays using oxygen-deficient TiO<sub>2</sub> nanoparticles as catalysts. *Nano Lett.* **15**, 403–409 (2015).
19. Yang, F. et al. Water-assisted preparation of high-purity semiconducting (1,4) carbon nanotubes. *ACS Nano* **11**, 186–193 (2017).
20. Ding, F., Harutyunyan, A. R. & Yakobson, B. I. Dislocation theory of chirality-controlled nanotube growth. *Proc. Natl Acad. Sci. USA* **106**, 2506–2509 (2009).
21. Liu, B., Wu, F., Gui, H., Zheng, M. & Zhou, C. Chirality-controlled synthesis and applications of single-wall carbon nanotubes. *ACS Nano* **11**, 31–53 (2017).
22. Zhu, Z. et al. Acoustic-assisted assembly of an individual monochromatic ultralong carbon nanotube for high on-current transistors. *Sci. Adv.* **2**, e1601572 (2016).
23. Zhang, S. et al. Arrays of horizontal carbon nanotubes of controlled chirality grown using designed catalysts. *Nature* **543**, 234–238 (2017).
24. Yang, F. et al. Chirality-specific growth of single-walled carbon nanotubes on solid alloy catalysts. *Nature* **510**, 522–524 (2014).
25. Sanchez-Valencia, J. R. et al. Controlled synthesis of single-chirality carbon nanotubes. *Nature* **512**, 61–64 (2014).
26. Zhao, Q., Xu, Z., Hu, Y., Ding, F. & Zhang, J. Chemical vapor deposition synthesis of near-zigzag single-walled carbon nanotubes with stable tube-catalyst interface. *Sci. Adv.* **2**, e1501729 (2016).
27. Han, J., Anantram, M. P., Jaffe, R. L., Kong, J. & Dai, H. Observation and modeling of single-wall carbon nanotube bend junctions. *Phys. Rev. B* **57**, 14983–14989 (1998).
28. Yao, Y. et al. Temperature-mediated growth of single-walled carbon-nanotube intramolecular junctions. *Nat. Mater.* **6**, 283–286 (2007).
29. Wang, J. et al. Observation of charge generation and transfer during CVD growth of carbon nanotubes. *Nano Lett.* **16**, 4102–4109 (2016).
30. Nasibulin, A. G. et al. Charging of aerosol products during ferrocene vapor decomposition in N<sub>2</sub> and CO atmospheres. *J. Phys. Chem. C* **112**, 5762–5769 (2008).
31. Gonzalez, D. et al. Single-walled carbon nanotube charging during bundling process in the gas phase. *Phys. Status Solidi.* **243**, 3234–3237 (2006).
32. Gonzalez, D. et al. Spontaneous charging of single-walled carbon nanotubes in the gas phase. *Carbon* **44**, 2099–2101 (2006).
33. Gonzalez, D. et al. Spontaneous charging of single-walled carbon nanotubes: a novel strategy for the selective substrate deposition of individual tubes at ambient temperature. *Chem. Mater.* **18**, 5052–5057 (2006).
34. Xiao, J. et al. Alignment controlled growth of single-walled carbon nanotubes on quartz substrates. *Nano Lett.* **9**, 4311–4319 (2009).
35. Ellison, G. B., Engelking, P. C. & Lineberger, W. C. An experimental determination of the geometry and electron affinity of CH<sub>3</sub><sup>-</sup>. *J. Am. Chem. Soc.* **100**, 2556–2558 (1978).
36. Zittel, P. F. et al. Laser photoelectron spectrometry of CH<sub>2</sub><sup>-</sup>. Singlet–triplet splitting and electron affinity of CH<sub>2</sub><sup>-</sup>. *J. Am. Chem. Soc.* **98**, 3731–3732 (1976).
37. Dresselhaus, M. S., Dresselhaus, G., Jorio, A., Souza Filho, A. G. & Saito, R. Raman spectroscopy on isolated single wall carbon nanotubes. *Carbon* **40**, 2043–2061 (2002).
38. He, Y. et al. Evaluating bandgap distributions of carbon nanotubes via scanning electron microscopy imaging of the Schottky barriers. *Nano Lett.* **13**, 5556–5562 (2013).
39. Li, J. et al. Direct identification of metallic and semiconducting single-walled carbon nanotubes in scanning electron microscopy. *Nano Lett.* **12**, 4095–4101 (2012).
40. Li, D. et al. Direct discrimination between semiconducting and metallic single-walled carbon nanotubes with high spatial resolution by SEM. *Nano Res.* **10**, 1896–1902 (2016).
41. Li, D. et al. Scanning electron microscopy imaging of single-walled carbon nanotubes on substrates. *Nano Res.* **10**, 1804–1818 (2017).
42. Lu, W. et al. Contactless characterization of electronic properties of nanomaterials using dielectric force microscopy. *J. Phys. Chem. C* **116**, 7158–7163 (2012).
43. Wang, X. et al. Fabrication of ultralong and electrically uniform single-walled carbon nanotubes on clean substrates. *Nano Lett.* **9**, 3137–3141 (2009).
44. Jian, M. et al. Volatile-nanoparticle-assisted optical visualization of individual carbon nanotubes and other nanomaterials. *Nanoscale* **8**, 13437–13444 (2016).
45. KANG, S. J. et al. High-performance electronics using dense, perfectly aligned arrays of single-walled carbon nanotubes. *Nat. Nanotechnol.* **2**, 230–236 (2007).
46. Parveen, S., Kumar, A., Husain, S. & Husain, M. Fowler Nordheim theory of carbon nanotube based field emitters. *Physica B* **505**, 1–8 (2017).

### Acknowledgements

We are grateful to L. Peng (Peking University), Y. Zhang (Tsinghua University), F. Ding (Ulsan National Institute of Science and Technology, Korea), Y. Xu (Tsinghua University, China) and X. Feng (University of Central Florida, USA) for discussions. This work is financially supported by the Basic Science Center Project of National Natural Science Foundation of China (NSFC) under grant no. 51788104, the NSFC (51727805, 51672152, 51472141), the National Key Research and Development Program of China (2017YFA0205800) and the Beijing Advanced Innovation Center for Future Chips (ICFC). Q. Ji and J. Kong acknowledge support from the STC Center for Integrated Quantum Materials, NSF grant DMR-1231319.

### Author contributions

J.W., X.J., Z.L., Z.Y. and H.W. contributed to experimental setup establishment. J.W., Z.L., G.Y. and J.L. contributed to CNT growth. J.W., P.L., J.K., Y.Wu, Y.Wei and K.J. contributed to theoretical analysis. J.W., J.Z., K.Z. and D.L. contributed to FET fabrication. J.W. contributed to Raman experiments. All authors discussed the results and wrote the paper.

### Competing interests

The authors declare no competing interests.

### Additional information

**Supplementary information** is available for this paper at <https://doi.org/10.1038/s41929-018-0057-x>.

**Reprints and permissions information** is available at [www.nature.com/reprints](http://www.nature.com/reprints).

**Correspondence and requests for materials** should be addressed to P.L. or J.K. or K.J.

**Publisher's note:** Springer Nature remains neutral with regard to jurisdictional claims in published maps and institutional affiliations.